8166 *J. Phys. Chem. A* **2003,** *107,* 8166−8176

Quantitative Modeling of Nonlinear Processes in Coherent Two-Dimensional Vibrational Spectroscopy†

John C. Wright,* Nicholas J. Condon, Keith M. Murdoch, Daniel M. Besemann, and Kent A. Meyer

Department of Chemistry, 1101 University Avenue, University of Wisconsin, Madison, Wisconsin 53706

Received: January 3, 2003; In Final Form: April 8, 2003

The line shapes and intensities in coherent multidimensional vibrational spectra are determined by amplitude level interference between different nonlinear processes. The relative amplitude and phase of each process is controlled by the transition moments and dephasing rates associated with each coherence in a nonlinear pathway. The important nonlinear pathways involve processes that are doubly vibrationally enhanced (DOVE) and nonresonant. The DOVE processes are sensitive to dephasing-induced resonances that change the appearance of two-dimensional spectral features. To understand how these contributions interfere to create a two-dimensional vibrational spectrum, line shapes were measured in the frequency domain for a set of model compounds over a range of vibrational frequencies. The amplitudes and dephasing rates for each pathway were determined by modeling spectra. By comparing the amplitudes with a deuteriobenzene internal standard, quantitative values were obtained for the DOVE processes. The results agree with recent ab initio calculations of the third-order DOVE susceptibilities, previous measurements of the concentration dependence, and estimates based on the absorption and Raman cross-sections of each resonance. The interference effects make the DOVE measurements sensitive to the sign of the transition moments.

Introduction

Coherent multidimensional vibrational spectroscopy (CMDVS) is based on driving multiple, coupled vibrational coherences by focusing coherent beams into a sample and measuring the radiating output coherence with frequency-domain or time-domain spectroscopic methods.[1,2] The methods are the vibrational analogue of multidimensional NMR methods.[3−6] Multidimensional vibrational spectroscopy has been studied by three-wave, four-wave, and six-wave mixing methods, although any nonlinear optical process is capable of CMDVS.[2,7,8] The methods differ in whether vibrational resonances are excited by single photon absorption/stimulated emission, two-photon Raman/two-photon absorption/emission, or three-photon hyper-Raman/hyper-Rayleigh transitions. For example, four-wave mixing methods have four transitions that can be used to excite vibrational resonances by four single-photon transitions as in stimulated photon echo methods or two single-photon transitions and one two-photon Raman transition as in the methods described in this paper.[2,8]

Doubly vibrationally enhanced (DOVE) four-wave mixing (FWM) spectroscopy was experimentally demonstrated with two single-photon infrared transitions and one Raman transition in an acetonitrile/deuteriobenzene mixture.[9−11] The experiments were performed by focusing two tunable, coherent, infrared beams (frequencies ω_1 and ω_2) and a visible beam (ω_3) into a sample and monitoring the nonlinear output beam intensity at $\omega_4 = \omega_1 - \omega_2 + \omega_3$ as a function of ω_1 and ω_2. In general, the spectra could contain contributions from nonresonant, singly vibrationally enhanced (SIVE),[12−14] and doubly vibrationally enhanced (DOVE) processes that can be modeled with conventional frequency domain expressions. The concentration dependence of the DOVE line shapes was fit to the no-pure-dephasing limit, where dephasing-induced resonances are absent and experimental values for the nonlinearities were defined by the fitting.[9] These values agreed with recent ab initio calculations of the acetonitrile DOVE nonlinearities.[15] DOVE spectra were also measured in acetonitrile/deuterioacetonitrile/deuteriobenzene mixtures in order to demonstrate the capabilities for selectively enhancing isotopomers in mixtures.[16] The two-dimensional experimental DOVE spectra of both mixtures were also simulated in the limit of no pure dephasing. Although there was qualitative agreement with the experimental spectra, the Lorentzian tails of the two-dimensional features were far more pronounced in the simulations than the experimental data.[16]

Pure dephasing is important for vibrational transitions, so it is expected that there will be important effects in the spectra. Prior et al.[17] and Andrews and Hochstrasser[18] showed that nonparametric processes often contained resonances that do not appear in spectra because destructive interference between different coherence pathways eliminate the resonances. However, they showed that if pure dephasing were present, the relative contributions from the interfering pathways changed so the quantum interference did not eliminate the resonances. These dephasing-induced resonances were called pressure-induced extra resonances in four-wave mixing (PIER4) for gas-phase samples[17] and dephasing-induced coherent emission (DICE) for condensed-phase samples.[18]

In this paper, we report more detailed experimental measurements of the frequency-dependent line shapes for acetonitrile (CH_3CN), deuterioacetonitrile (CD_3CN), and deuteriobenzene (C_6D_6) model mixtures as well as simulations of the line shapes. The simulations demonstrate that dephasing-induced resonances play a dominant role in CMDVS and their inclusion narrows the tails on DOVE resonances and produces quantitative agreement with experimental spectra. Modeling of the entire

---

† Part of the special issue “A. C. Albrecht Memorial Issue”.

* Corresponding author. E-mail: wright@chem.wisc.edu.

10.1021/jp034018i CCC: $25.00

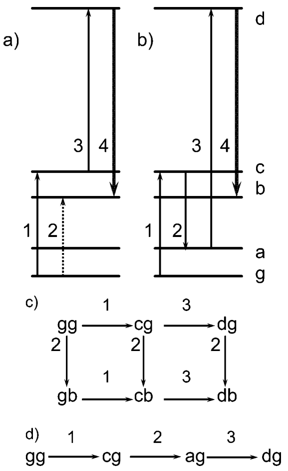

Figure 1. Liouville coherence pathways (a and b) and the wave mixing energy level (WMEL) (c and d) diagrams for DOVE-IR (a and c) and DOVE-Raman (b and d). The numbers label the frequencies of the excitation beams while the letters designate the molecular states. The double letters in the WMEL diagrams designate the diagonal populations and off-diagonal coherences of the density matrix.

two-dimensional DOVE spectra allows one to extract $\chi^{(3)}$ values for all the nonlinear processes that contribute appreciably to the DOVE spectra. These values also agree excellently with ab initio calculations[15] and estimates based on the linear absorption and Raman cross-section measurements of the transitions.[9]

Theory

Figure 1 shows the Liouville coherence pathways[2,19–22] and the wave mixing energy level (WMEL) diagrams[23] for the DOVE-IR and DOVE-Raman processes that dominate the two-dimensional DOVE spectra. The DOVE-IR process on the left involves two infrared excitations from the ground state in the first two steps. The DOVE-Raman process on the right involves two consecutive infrared transitions that correspond to a resonance Raman process that is enhanced by a vibrational state instead of the more typical electronic state. The numbers in the WMEL diagrams label the frequencies of the different beams, while the two letters designate the states in the density matrix elements, ρ_{ij} ($\rho_{ij} \equiv c_i c_j^*$), that describe each coherence. The numbers do not label the particular transitions. For the DOVE-IR process, there are three pathways from the initial ρ_{gg} population to the emitting ρ_{db} coherence but only the gg → cg → cb → db (labeled α) and the gg → gb → cb → db (labeled β) pathways have two vibrational resonances.[24,25] In the rotating wave approximation, the steady-state expressions for the two ρ_{db} coherence pathways are

$$\rho_{db}^{\alpha} = -\sum_{g,b,c,d=\text{allstates}} \frac{\Omega_{gc}\Omega_{cd}\Omega_{gb}}{8\Delta_{cg}\Delta_{cb}\Delta_{db}} \rho_{gg} \exp\{i[(k_1 - k_2 + k_3)z - (\omega_1 - \omega_2 + \omega_3)t]\} \quad (1)$$

$$\rho_{db}^{\beta} = \sum_{g,b,c,d=\text{allstates}} \frac{\Omega_{gc}\Omega_{gb}\Omega_{cd}}{8\Delta_{bg}^{*}\Delta_{cb}\Delta_{db}} \rho_{gg} \exp\{i[(k_1 - k_2 + k_3)z - (\omega_1 - \omega_2 + \omega_3)t]\} \quad (2)$$

For the DOVE-Raman process, there is a single pathway (gg → cg → ag → dg) from the initial ρ_{gg} population to the ρ_{dg} output coherence given by

$$\rho_{dg} = \sum_{g,a,c,d=\text{allstates}} \frac{\Omega_{gc}\Omega_{ca}\Omega_{ad}}{8\Delta_{cg}\Delta_{ag}\Delta_{dg}} \rho_{gg} \exp\{i[(k_1 - k_2 + k_3)z - (\omega_1 - \omega_2 + \omega_3)t]\} \quad (3)$$

In these equations $\Delta_{cg} \equiv \omega_{cg} - \omega_1 - i\Gamma_{cg}$, $\Delta_{cb} \equiv \omega_{cb} - \omega_1 + \omega_2 - i\Gamma_{cb}$, $\Delta_{db} \equiv \omega_{db} - \omega_4 - i\Gamma_{db}$, $\Delta_{bg}{}^* \equiv \omega_{bg} - \omega_2 + i\Gamma_{bg}$, $\Delta_{ag} \equiv \omega_{ag} - \omega_1 + \omega_2 - i\Gamma_{ag}$, $\Delta_{dg} = \omega_{dg} - \omega_4 - i\Gamma_{dg}$, and $\Omega_{i,j}$, μ_{ij}, ω_{ij}, and $\Gamma_{i,j}$ are the Rabi frequency ($\Omega_{i,j} \equiv \bar{\boldsymbol{\mu}}_{i,j}\bar{\boldsymbol{E}}/\hbar$), transition moment, transition frequency, and dephasing rate for the i−j transition, respectively.

To compare the experimental measurements with theoretical simulations, all of the factors that are constant or nearly constant in eqs 1−3 are combined into adjustable fitting constants, A_i. Although the summations over the g, a, b, c, and d states include both electronic and vibrational states, only the vibrational states contribute observable spectral features in CMDVS over the typical infrared frequency ranges. The electronic state contributions do not change appreciably in spectral scans, so one can suppress their frequency dependence and incorporate them as constants. The infrared vibrational state contributions are written explicitly with v, v′, and v″ labels, and excited electronic states are incorporated into the *A* values. Although v, v′, and v″ can represent any vibrational state, v and v′ represent fundamental modes (for the a and b states) and v″ represents a combination band of v and v′ for this paper (for the c state). The nonresonant, SIVE, and DOVE contributions from eqs 1−3 are then

$$\rho_{ev'}^{\alpha} = -\sum_{v,v',v''=\text{allvibrationalstates}} \left(A_{NR}^{\alpha} + \frac{A_{v''g}}{\Delta_{v''g}} + \frac{A_{v''g,v''v'}}{\Delta_{v''g}\Delta_{v''v'}} \right) \rho_{gg} \exp\{i[(k_1 - k_2 + k_3)z - (\omega_1 - \omega_2 + \omega_3)t]\} \quad (4)$$

$$\rho_{ev'}^{\beta} = \sum_{v,v',v''=\text{allvibrationalstates}} \left(A_{NR}^{\beta} + \frac{A_{v'g}}{\Delta_{v'g}^{*}} + \frac{A_{v'g,v''v'}}{\Delta_{v'g}\Delta_{v''v'}{}^{*}} \right) \rho_{gg} \exp\{i[(k_1 - k_2 + k_3)z - (\omega_1 - \omega_2 + \omega_3)t]\} \quad (5)$$

$$\rho_{e'g} = \sum_{v,v',v''=\text{allvibrationalstates}} \left(A_{NR}^{e''g} + \frac{A_{v''g}}{\Delta_{v''g}} + \frac{A_{v''g,vg}}{\Delta_{v''g}\Delta_{vg}} \right) \rho_{gg} \exp\{i[(k_1 - k_2 + k_3)z - (\omega_1 - \omega_2 + \omega_3)\mathrm{t}]\} \quad (6)$$

The output coherences, $\rho_{mn}{}^{i}$, from each sample component, *i*, creates a nonlinear polarization given by

$$P_i = \chi_i^{(3)} E^3 = N_i F \sum_{m,n=\text{allstates}} \mu_{mn}\rho_{mn} = N_i F \gamma_i \quad (7)$$

where $\chi_i{}^{(3)}$, N_i, γ_i, and *F* are the third-order susceptibility of component *i*, its molecular concentration, its hyperpolarizability, and the local field correction factor, respectively.[2] The nonlinear polarization launches the electromagnetic field that is detected as an intensity. In the experimental work, the nonlinear polarization was described by the third-order susceptibility, $\chi^{(3)}$. It was measured interferometrically by the method developed by Levenson and Bloembergen,[26,27] where the dispersive line shapes of a Raman resonance and a nonresonant background allows a comparison between Raman resonances and the Raman resonance of an internal $\chi^{(3)}$ standard.[9]

If one now monitors the output signal at $\omega_4 = \omega_1 - \omega_2 + \omega_3$, the $\chi^{(3)}$ frequency dependence of component *i* will be given

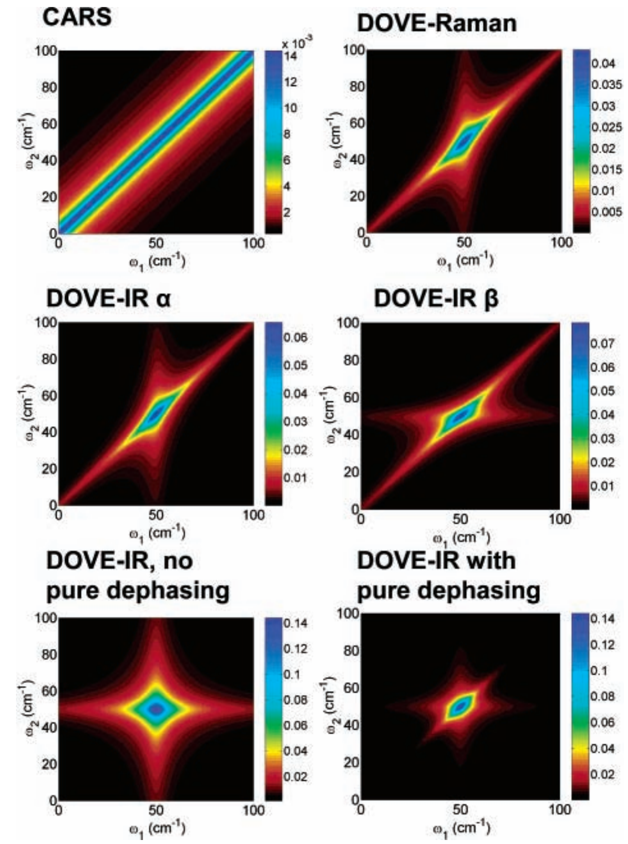

Figure 2. Magnitude of the important frequency-dependent processes in eq 8 is plotted as a function of ω_1 and ω_2 to show their 2D spectral signature.

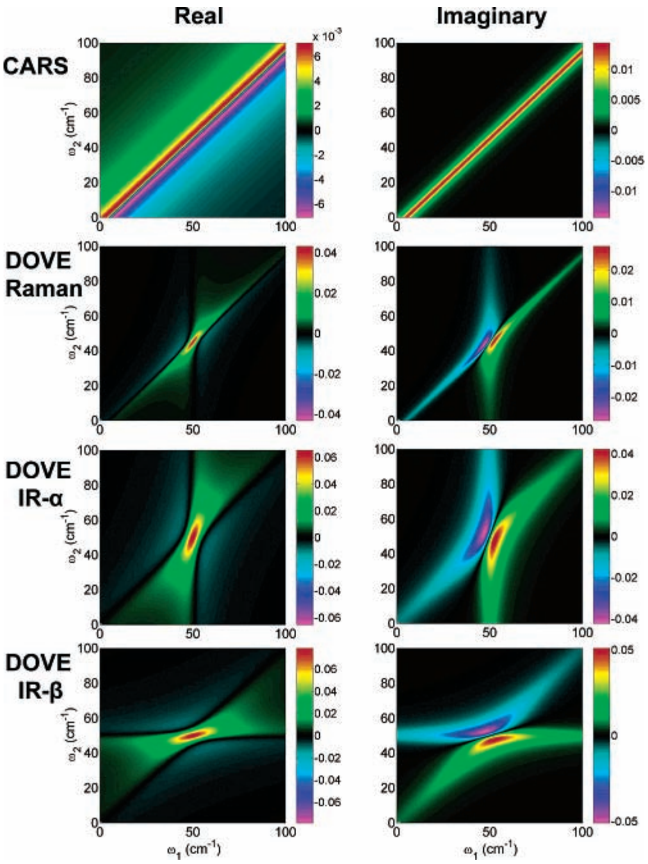

Figure 3. Real and imaginary values for the important frequency-dependent processes in eq 8 are plotted as a function of ω_1 and ω_2. The color bars indicate the amplitude.

by the sum of the contributions from all states of each component:

$$\chi_i^{(3)} = N_i F \sum_{\mathrm{v,v',v''=allvibrationalstates}} A_{\mathrm{NR}} + \frac{A_{\mathrm{CARS}}}{\Delta_{\mathrm{vg}}} + \frac{A_{\mathrm{SIVE1}}}{\Delta_{\mathrm{v''g}}} + \frac{A_{\mathrm{SIVE2}}}{\Delta^*_{\mathrm{v'g}}} - \frac{A_{\mathrm{DOVE-IR\alpha}}}{\Delta_{\mathrm{v''g}}\Delta_{\mathrm{v''v'}}} + \frac{A_{\mathrm{DOVE-IR\beta}}}{\Delta^*_{\mathrm{v'g}}\Delta_{\mathrm{v''v'}}} + \frac{A_{\mathrm{DOVE-Raman}}}{\Delta_{\mathrm{v''g}}\Delta_{\mathrm{vg}}} \quad (8)$$

where the other constants have been absorbed into the A constants in the numerator.[9] The first term represents all the nonresonant contributions, the second term represents the coherent anti-Stokes Raman scattering (CARS) contribution from all the single Raman resonances, the third and fourth terms represent all the SIVE resonances that depend on ω_1 or ω_2, respectively,[12-14] the fifth and sixth terms represent the two DOVE-IR pathways, and the last term represents the DOVE-Raman pathway. The macroscopic polarization is the sum of the polarizations created by each sample component, $\chi^{(3)} = \Sigma_{i=\mathrm{allcomponents}}\, \chi_i^{(3)}$.

Figure 2 plots the magnitude of the important vibrationally resonant $\boldsymbol{\chi}^{(3)}$ values in eq 8, and Figure 3 shows the real and imaginary values. The parameter values used in these simulations correspond with those used in the data simulations reported later in this paper. Each process has a unique spectral signature. For example, the four fundamental processes each have a diagonal feature from the Δ_{ag} or Δ_{cb} resonances that depend on $\omega_1 - \omega_2$. The DOVE processes have an additional horizontal or vertical feature from the second resonance that depends on either ω_1 or ω_2 alone. The character of the spectral signature can change appreciably because of amplitude level interferences between processes as can be seen in the bottom set of spectra in Figure 2.[28] For example, the interference between the two DOVE-IR pathways can actually eliminate the strong diagonal signature of the $\Delta_{\mathrm{v''v'}}$ resonance in each pathway as seen in the spectrum with no pure dephasing. If there is dephasing, the diagonal feature returns but the line shape is quite different.

To understand this behavior more fully, note the shapes of the imaginary parts of the diagonal features for the two DOVE-IR pathways shown in Figure 3. They have opposite signs and will destructively interfere. The amount of destructive interference is controlled by the relative dephasing rates. If $A_{\mathrm{DOVE-IR\alpha}} = A_{\mathrm{DOVE-IR\beta}}$, one can rewrite the two DOVE-IR terms in eq 8 as

$$\frac{A_{\mathrm{DOVE-IR}}}{\Delta_{\mathrm{v''g}}\Delta^*_{\mathrm{v'g}}}\left(1 + \frac{i\Gamma^{\mathrm{g}}_{\mathrm{v''v'}}}{\Delta_{\mathrm{v''v'}}}\right) \quad (9)$$

where $\Gamma_{\mathrm{v''v'}}{}^{\mathrm{g}} \equiv \Gamma_{\mathrm{v''v'}} - \Gamma_{\mathrm{v''g}} - \Gamma_{\mathrm{v'g}}$. One can also show that if

$$\Gamma_{\mathrm{v''v'}} \equiv \frac{\Gamma_{\mathrm{v''v''}} + \Gamma_{\mathrm{v'v'}}}{2} + \Gamma^*_{\mathrm{v''v'}} \quad (10)$$

where $\Gamma^*_{\mathrm{v''v'}}$ is the pure dephasing rate of the $\rho_{\mathrm{v''v'}}$ coherence and Γ_{vv} is the population relaxation rate of the v-state population, then $\Gamma^{\mathrm{g}}_{\mathrm{v''v'}} = \Gamma^*_{\mathrm{v''v'}} - \Gamma^*_{\mathrm{v''g}} - \Gamma^*_{\mathrm{v'g}} - \Gamma_{\mathrm{gg}}$. Since $\Gamma^{\mathrm{g}}_{\mathrm{v''v'}}$ vanishes in the limit of no pure dephasing, the $\Delta_{\mathrm{v''v'}}$ resonance will disappear. If there is pure dephasing, it is present so this resonance is an example of a dephasing-induced resonance.[17,18] Note that the $\Delta_{\mathrm{v''v'}}$ resonance also vanishes if $\Gamma_{\mathrm{v''v'}} = \Gamma_{\mathrm{v''g}} + \Gamma_{\mathrm{v'g}}$. The bottom spectra in Figure 2 show the spectral shapes when there is no pure dephasing and when pure dephasing is

TABLE 1: Pure Dephasing Rates for Different Coherences, with the Assumption That v″ Is a Combination Band of Modes v and v′

Γ	general pure dephasing rate	no correlation	complete correlation
Γ^*_{vg}	$\Gamma^*_{\mathrm{vg}} = A_{\mathrm{v}}^2\Phi_{\mathrm{vv}} + A_{\mathrm{g}}^2\Phi_{\mathrm{gg}} - A_{\mathrm{v}}A_{\mathrm{g}}(\Phi_{\mathrm{vg}} + \Phi_{\mathrm{gv}})$	$(A_{\mathrm{v}}^2 + A_{\mathrm{g}}^2)\Phi$	$(A_{\mathrm{v}} - A_{\mathrm{g}})^2\Phi$
$\Gamma^*_{\mathrm{v'g}}$	$\Gamma^*_{\mathrm{v'g}} = A_{\mathrm{v'}}^2\Phi_{\mathrm{v'v'}} + A_{\mathrm{g}}^2\Phi_{\mathrm{gg}} - A_{\mathrm{v'}}A_{\mathrm{g}}(\Phi_{\mathrm{v'g}} + \Phi_{\mathrm{gv'}})$	$(A_{\mathrm{v'}}^2 + A_{\mathrm{g}}^2)\Phi$	$(A_{\mathrm{v'}} - A_{\mathrm{g}})^2\Phi$
$\Gamma^*_{\mathrm{v''g}}$	$\Gamma^*_{\mathrm{vg}} + \Gamma^*_{\mathrm{v'g}} + 2A_{\mathrm{g}}^2\Phi_{\mathrm{gg}} + A_{\mathrm{v}}A_{\mathrm{v'}}(\Phi_{\mathrm{vv'}} + \Phi_{\mathrm{v'v}}) - A_{\mathrm{v}}A_{\mathrm{g}}(\Phi_{\mathrm{vg}} + \Phi_{\mathrm{gv}}) - A_{\mathrm{v'}}A_{\mathrm{g}}(\Phi_{\mathrm{v'g}} + \Phi_{\mathrm{gv'}})$	$\Gamma^*_{\mathrm{vg}} + \Gamma^*_{\mathrm{v'g}} + 2A_{\mathrm{g}}^2\Phi$	$\Gamma^*_{\mathrm{vg}} + \Gamma^*_{\mathrm{v'g}} + 2(\Gamma^*_{\mathrm{vg}}\,\Gamma^*_{\mathrm{v'g}})^{1/2}$
$\Gamma^*_{\mathrm{v''v'}}$	Γ^*_{vg}	Γ^*_{vg}	Γ^*_{vg}

important. Note the lack of diagonal character when there is no pure dephasing and note also the more compact spectral shape that results from the interference of the two DOVE-IR pathways when pure dephasing is important.

The DOVE-IR and DOVE-Raman processes can interfere as well. If they have the same amplitudes in eq 8 and if there is no anharmonicity, then $\Delta_{\mathrm{v''v'}} = \Delta_{\mathrm{vg}}$ where state v″ is a combination band involving states v′ and v. In this situation, the two DOVE-IR and the DOVE-Raman terms combine to give

$$\chi^{(3)}_{\mathrm{DOVE-IR}\alpha} + \chi^{(3)}_{\mathrm{DOVE-IR}\beta} + \chi^{(3)}_{\mathrm{DOVE-Raman}} = \frac{A}{\Delta^*_{\mathrm{v'g}}\Delta_{\mathrm{vg}}} \quad (11)$$

The 2D feature in this case has the spectral signature of the β pathway for DOVE-IR. Of course, reaching this limit is not reasonable because if the combination band lacked anharmonicity, the combination band would lose intensity and the 2D feature would vanish.

If there is anharmonicity, the DOVE-Raman/DOVE-IR features appear separately and the ratio of their nonlinearities is given by

$$\frac{\chi^{(3)}_{\mathrm{DOVE-IR}}}{\chi_{\mathrm{DOVE-Raman}}} = -\frac{A_{\mathrm{DOVE-IR}}\Gamma_{\mathrm{vg}}}{A_{\mathrm{DOVE-Raman}}\Gamma_{\mathrm{v''v'}}}\left(1 + \frac{\Gamma_{\mathrm{v''g}}}{\Gamma_{\mathrm{v'g}}}\right) \quad (12)$$

If the transition moments and the dephasing rates for DOVE-IR and DOVE-Raman are identical, this ratio is -2.

There is also interference between the DOVE-Raman and CARS features as can be clearly seen from the imaginary parts of their $\chi^{(3)}$ in Figure 3. These two processes combine to give

$$\chi^{(3)}_{\mathrm{Raman}} + \chi^{(3)}_{\mathrm{CARS}} = \frac{A_{\mathrm{CARS}}}{\Delta_{\mathrm{vg}}}\left(1 + \frac{A_{\mathrm{DOVE-Raman}}}{A_{\mathrm{CARS}}\Delta_{\mathrm{v''g}}}\right) \quad (13)$$

If ω_1 is lower than $\omega_{\mathrm{v''g}}$ and the detuning is appreciably larger than the line width, $\Gamma_{\mathrm{v''g}}$, the two terms will interfere constructively or destructively depending upon whether $A_{\mathrm{DOVE-Raman}}/A_{\mathrm{CARS}}$ is positive or negative, respectively. Similarly, if ω_1 is higher than $\omega_{\mathrm{v''g}}$, the interference will reverse. One therefore expects that the DOVE-Raman contribution will enhance the CARS feature on one side of the $\rho_{\mathrm{v''g}}$ resonance and depress it on the other side. This behavior is particularly clear when the signs of the diagonal features of these two processes are compared in Figure 3.

There can also be changes in the asymmetry of the line shape if there is interference with a background.[26,29] Interference with a background typically creates a dispersive line shape, and the character of the asymmetry depends on the relative signs of the resonance and background. Since $\Delta_{\mathrm{v''g}}$ changes sign on either side of the g → v″ resonance, the asymmetry of the Δ_{vg} resonance can reverse when $|A_{\mathrm{DOVE-Raman}}/(A_{\mathrm{CARS}}\Delta_{\mathrm{v''g}})| > 1$.

Theoretical calculations can define the signs of the $\chi^{(3)}$ values for each of the nonlinear processes. Ab initio calculations by Kwak et al.[15] have determined the magnitude and signs of the important nonlinear processes in acetonitrile. Calculations of the $\chi^{(3)}$ values require determination of two infrared absorption transition moments and a Raman transition moment. The infrared transition moment for a fundamental and a combination band requires calculation of $\partial\mu/\partial Q_i$, $\partial^2\mu/\partial Q_i\partial Q_j$, and $\partial^3 V/\partial Q_i\partial Q_j\partial Q_k$ in order to properly account for electrical and mechanical anharmonicities. The Raman transition moment for a fundamental requires calculation of $(\partial\alpha/\partial Q_i)$. Here, Q_i is a normal-mode coordinate, V is the molecular potential, and α is the polarizability. The calculations showed that the transition moments for the two infrared transitions are positive but the transition moment for the Raman transition is negative. The sign of the transition moment is not normally observed in an infrared absorption or a Raman transition because the transition moments enter quadratically. However, the signs enter the $\chi^{(3)}$ expression linearly in three-laser, nonlinear experiments so the signs are measurable. The nonresonant $\chi^{(3)}$ involves two amplitude-level two-photon transitions so the two photon transition moments enter as the square and an overall positive sign results. Similarly, a CARS $\chi^{(3)}$ typically involves two amplitude-level Raman transitions so the Raman transition moments enter as the square and an overall positive sign results. The DOVE-Raman $\chi^{(3)}$ involves two amplitude-level infrared transitions and one amplitude-level Raman transition so the product of the three transition moments will have the opposite sign from the CARS product. The DOVE-IR $\chi^{(3)}$ involves the same product of transition moments as DOVE-Raman but its $\chi^{(3)}$ has the opposite sign because it has one bra side transition (see eq 1). Thus, a resonant CARS line and an off-resonance DOVE-Raman line can interfere destructively if ω_1 is lower than $\omega_{\mathrm{v''g}}$ and constructively if it is higher, as is the case in Figure 3.

If v″ is a combination band of the v and v′ modes, the dephasing rates $\Gamma_{\mathrm{v''g}}$, $\Gamma_{\mathrm{v'g}}$, Γ_{vg}, and $\Gamma_{\mathrm{v''v'}}$ are related. Their relationship affects the line shapes and relative intensities because of the interference between coherence pathways. As shown previously,[28] the pure dephasing rate, $\Gamma_{ij}{}^*$, in eq 10 is given by

$$\Gamma_{ij}{}^* = \int_0^\infty \mathrm{d}\tau\, [\Delta\omega_i(\tau) - \Delta\omega_j(\tau)][\Delta\omega_i(0) - \Delta\omega_j(0)] \quad (14)$$

where $\Delta\omega_i(\tau)$ is the instantaneous frequency fluctuation about the ω_i mean frequency. If $\varphi(t)$ is a stochastic function such that $\langle\varphi_i(t)\varphi_i(0)\rangle = 1$ when $t = 0$, we can define $\Delta\omega_i(\tau) \equiv A_i\varphi_i(t)$ where A is the amplitude of the frequency fluctuation. We can also define a correlation function, $\Phi_{ij} \equiv \int_0^\infty \mathrm{d}\tau\ \langle\phi_i(\tau)\phi_{\mathrm{i}}(0)\rangle$. One can then determine the pure dephasing rates for the different coherences in terms of the correlation functions and the amplitudes. The values for the general case as well as the extreme limits of no correlation where $\Phi_{ij} = \Phi\delta_{ij}$ and complete correlation where $\Phi_{ij} = \Phi$ are summarized in Table 1. Together with eq 10, these relationships define the ranges for the observed dephasing rates. The Γ_{vg}, $\Gamma_{\mathrm{v'g}}$, and $\Gamma_{\mathrm{v''g}}$ dephasing rates are measurable from infrared spectra when the line widths are determined by homogeneous broadening.

Table 1 provides guidance in evaluating the relative importance of DOVE-IR and DOVE-Raman processes by use of eqs 10 and 12. If the population relaxation rates are not important, one expects $\Gamma_{\mathrm{v''v'}} = \Gamma_{\mathrm{vg}}$, but if they are important, $\Gamma_{\mathrm{v''v'}} > \Gamma_{\mathrm{vg}}$,

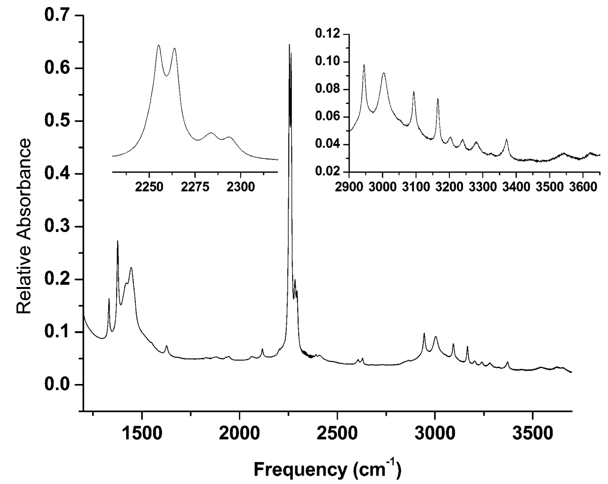

Figure 4. Absorption spectrum of the 48%:48%:4% CH_3CN/CD_3CN/C_6D_6 mixture. The two insets expand the range used for the nonlinear experiments.

since the combination band has a higher energy and will have additional relaxation pathways relative to the fundamental. In addition, one expects that $\Gamma_{v''g}/\Gamma_{v'g} > 1$ so the $\chi_{DOVE-IR}/\chi_{DOVE-Raman}$ ratio in eq 12 can be greater or smaller than -2 depending on the relative dephasing rate.

Experimental Section

The experimental methods were described previously.[9,25,30,31] Briefly, a Nd:YAG laser with 3.5 ns and 450 mJ pulses of 1064 nm light excites two optical parametric oscillator/optical parametric amplifier (OPO/OPA) systems to produce two independently tunable midinfrared pulses, ω_1 and ω_2. The Nd:YAG laser is frequency-doubled to provide the ω_3 beam. The signal beams from the OPOs are directed into a hollow cathode lamp for wavelength calibration via the optogalvanic effect. The ω_1 beam intensity is monitored throughout each scan. The three beams are focused into a flat, 140 μm thick fused silica capillary with the 80 μm thick sample. The ω_2 and ω_3 beams were set at 8° and $-0.5°$ external angles relative to the ω_1 beam in order to provide phase matching. Calculations of the internal phase matching angles accounted for the changes in angle from refraction at the glass interfaces. After the sample, the three excitation beams are rejected by spatial and spectral filters, and the signal beam is directed into a scanning double monochromator and detected with a photomultiplier. Two-dimensional spectra are acquired by synchronously scanning ω_1 and ω_4 for each choice of ω_2. A computer controls the scanning, data acquisition, and corrections for the ω_1 beam's intensity fluctuations. To correct for experimental drift in phase matching, beam overlap, changes in mode profiles, and other unknown factors, the spectra are normalized relative to a C_6D_6 CARS line at 944 cm^{-1}, which acts as an internal standard. This approach assumes that the Raman line is not enhanced by other resonances within the frequency range.

Results

The infrared spectrum of a 48:48:4 mol % CH_3CN/CD_3CN/C_6D_6 mixture is shown in Figure 4. The insets expand the frequency ranges that include the DOVE experiments. Table 2 summarizes the line positions, line widths, and molar absorptivities for the vibrational modes of interest in this work. It also includes the frequencies used in simulations of the data. The differences are caused by small frequency calibration errors. The table does not include shoulders on the ν_2 and ν_4 mode's transitions from unresolved $\nu_g \rightarrow \nu_i + \nu_8$ hot bands.[32]

TABLE 2: Frequencies, Line Widths, and Relative Amplitude for Transitions in Acetonitrile, Deuteroacetonitrile, and Deuterobenzene

	frequency[a] (cm^{-1})	Γ^b (cm^{-1})	Γ^c (cm^{-1})	molar absorptivity[b] (L mol^{-1} cm^{-1})	simulation frequency[d] (cm^{-1})	simulation Γ^d (cm^{-1})
			CH_3CN Mode			
ν_4	917	3.1		9.15	916.8	2.5
ν_3	1376	4.9		20.2		
ν_2	2254	2.9	4.3	41.7	2254.5	3.9
$\nu_3 + \nu_4$	2293	6.4	4.9	7.8	2293.7	6.4
ν_1	2944	6.0	6.8	6.34		
ν_5	3002	12.7	15.3	6.35		
$\nu_2 + \nu_4$	3165	5.2	4.2	2.52	3163.7	4.7
$\nu_3 + 2\nu_4$	3203	6.4	5.3	0.8	3201.1	7.1
$\nu_2 + \nu_3$	3632[b]	3.9		0.064		
			CD_3CN Mode			
ν_4					827.6	2.6
ν_2	2264	3.8	3.8	41.1	2265.6	2.9
$\nu_2 + \nu_4$	3095	5.3	6.8	2.17	3089.1	6.6
			C_6D_6 Mode			
ν_2	944				944	2.1

[a] Reference 32. [b] Reference 37 and this work. [c] Fits to absorption spectra from this work. [d] Least-squares fitting parameters used for nonlinear simulations in this work.

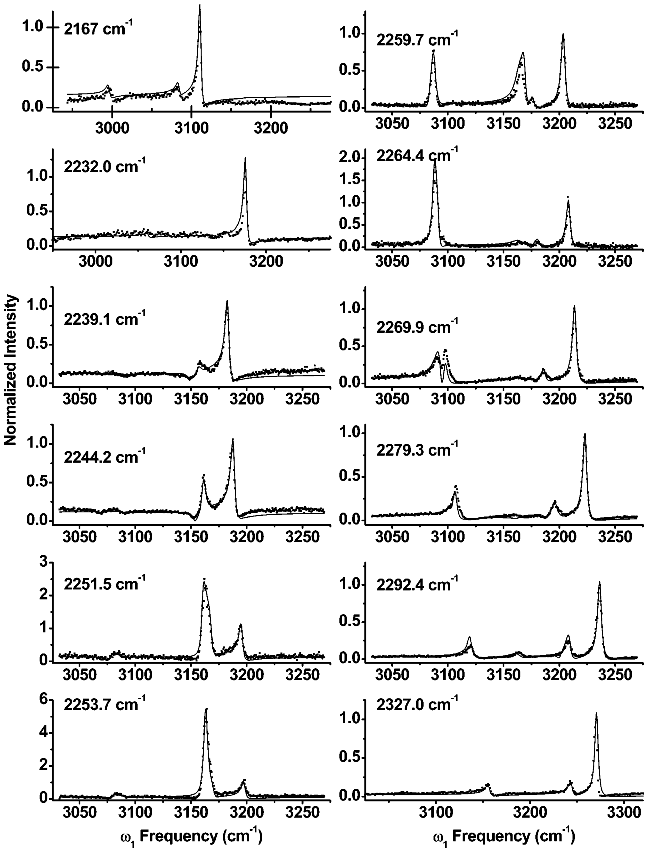

Figure 5. Nonlinear DOVE spectra where ω_1 was scanned for a series of ω_2 values that are indicated on each spectrum.

Figure 5 shows representative nonlinear DOVE spectra when ω_2 is set to the different frequencies indicated in the figure and ω_1 is scanned. All the spectra contain CARS peaks from the C_6D_6 $\omega_1 - \omega_2 = 944$ cm^{-1} ν_1 ring breathing mode[33] (peak on right for each spectrum) and the ν_4 C−C stretch modes of the CD_3CN and CH_3CN at $\omega_1 - \omega_2 = 828$ and 917 cm^{-1}, respectively.[32] The spectra have all been scaled so the peak intensity of the C_6D_6 944 cm^{-1} line is 1. The relative intensities of these peaks are best seen in the spectra at $\omega_2 = 2167$ and 2327 cm^{-1} because ω_2 is far from vibrational resonances that enhance the peaks. The peaks are asymmetric with a normal positively dispersive line shape because there is amplitude-level interference between the Raman resonance and the nonresonant background that enhances the low-energy side of the peak and suppresses the high-energy side. One can see that the CD_3CN 828 cm^{-1} and CH_3CN 917 cm^{-1} mode peaks have the same intensities relative to each other, but both are small compared to the more intense 944 cm^{-1} C_6D_6 peak.

As ω_2 is moved into the region of DOVE resonances, there are changes in the relative intensities and shapes of the CD_3CN and CH_3CN lines. In addition, new lines appear. For example, as ω_2 increases into the range where DOVE processes begin to contribute, the 828 and 917 cm^{-1} lines are first suppressed and later enhanced as the DOVE-Raman and CARS processes interfere. The line shape asymmetry of the enhanced line reverses so it becomes negatively dispersive (i.e., the low-energy side of the line is suppressed). A new line then grows in as the DOVE-IR process becomes important. Further increases in ω_2 lead to a decline in the DOVE-IR line. The 828 and 917 cm^{-1} lines remain enhanced but the line asymmetry again reverses so they return to positively dispersive line shapes.

These effects are seen throughout the range of spectra in Figure 5. In each spectrum, the C_6D_6 944 cm^{-1} line appears on the right-hand side. Since it is not enhanced by a second resonance, it is a convenient intensity reference. The suppression of the CARS features by the DOVE-Raman resonance is already clear in the $\omega_2 = 2232.0$ cm^{-1} spectrum. For the $\omega_2 = 2239.1$ cm^{-1} spectrum, the $\omega_1 - \omega_2 = 828$ cm^{-1} line is suppressed but the 917 cm^{-1} line has reappeared and is enhanced. The accompanying line-shape changes become clear in the $\omega_2 = 2244.2$ cm^{-1} spectrum where the 917 and 944 cm^{-1} lines have opposite dispersions. In the $\omega_2 = 2251.5$ cm^{-1} spectrum, the new CH_3CN DOVE-IR line can be seen appearing on the left shoulder of the 917 cm^{-1} line. This line dominates the spectrum when $\omega_2 = 2253.7$ cm^{-1}. One can see that the 828 cm^{-1} line is also enhanced in this spectrum. When $\omega_2 = 2259.7$ cm^{-1}, the 828 cm^{-1} line's enhancement from the CD_3CN DOVE-Raman and its unresolved DOVE-IR line is a clear feature on the left side. In addition, the CH_3CN DOVE-IR feature remains enhanced at $\omega_1 = 3164$ cm^{-1}, and the CH_3CN DOVE-Raman/CARS 917 cm^{-1} feature appears as a weak line on the right side of the CH_3CN DOVE-IR line at $\omega_1 = 3177$ cm^{-1}. The CH_3CN DOVE-IR and DOVE-Raman lines have almost disappeared in the $\omega_2 = 2264.4$ cm^{-1} spectrum, and the CD_3CN DOVE-IR line at $\omega_1 = 3089$ cm^{-1} has reached its maximum intensity. The CD_3CN DOVE-Raman line at $\omega_1 = 3096$ cm^{-1} is also visible but weak. This line grows, however, as ω_2 is incremented to 2269.9 cm^{-1} while the CD_3CN DOVE-IR line decreases. In the $\omega_2 = 2279.3$ cm^{-1} spectrum, one now sees the enhancement in the line at $\omega_1 = 3197$ cm^{-1} from the second set of CH_3CN DOVE-IR and DOVE-Raman resonances at ($\omega_1 = \nu_3 + 2\nu_4$, $\omega_2 = \nu_3 + \nu_4$) and ($\omega_1 = \nu_3 + 2\nu_4$, $\omega_1 - \omega_2 = \nu_4$), respectively. This feature reaches a maximum in the $\omega_2 = 2292.4$ cm^{-1} spectrum.

Figure 6 shows a two-dimensional contour plot of this same data so the relationships between the spectral features can be seen more clearly. The spectrum is dominated by the two strong DOVE-IR peaks of CD_3CN and CH_3CN and the three diagonal ridges of the C_6D_6, CD_3CN, and CH_3CN CARS and DOVE-Raman transitions. The weaker DOVE features discussed above are also visible. Note that the compact shape of the DOVE-IR peaks does not match the star shapes that are characteristic of the no-pure-dephasing limit (see bottom left of Figure 2).

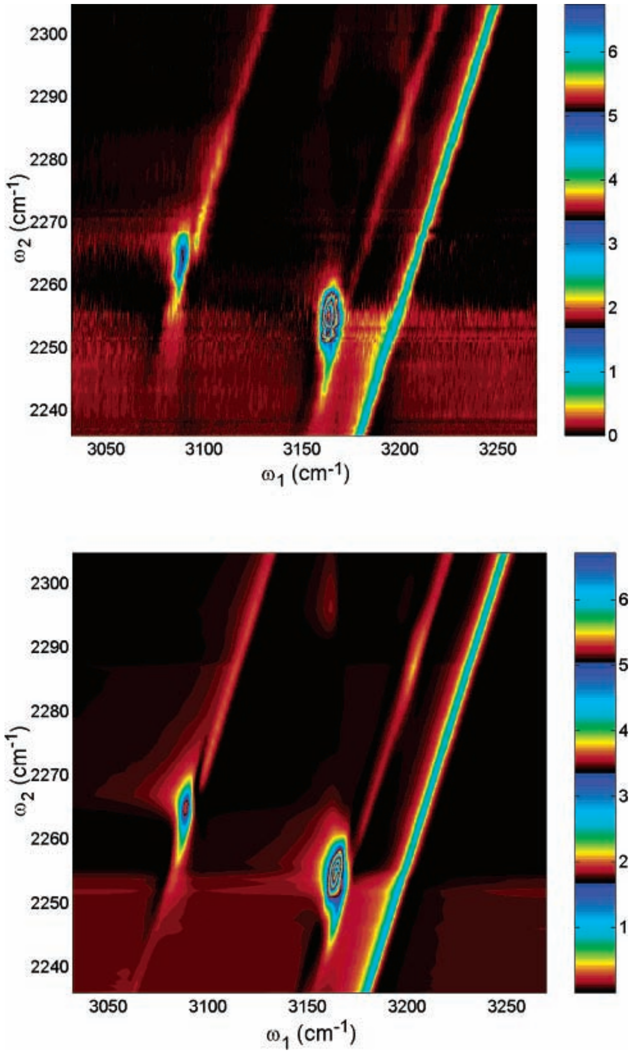

Figure 6. Experimental (top) and simulated (bottom) two-dimensional vibrational spectra of the entire series of ω_1 and ω_2 values. The spectra are normalized to the C_6D_6 944 cm^{-1} CARS line on the right side. The color bar indicates four cycles of color to accentuate the dynamic range of intensities so features near the baseline appear more clearly.

It is also interesting to examine the possible coupling between the C−H and C≡N modes. Ab initio calculations show that there should be small amounts of coupling between these modes.[15] Figure 7 shows spectra that include the region where ω_1 matches the C−H stretch fundamentals and ω_2 matches the C≡N fundamental at 2254 cm^{-1} as well as comparison spectra where ω_2 is higher and lower than the resonance. Comparison of the spectra shows there are no features at 2944 and 3002 cm^{-1}, the frequencies of the C−H fundamentals, so it is clear that any vibrational enhancements are smaller than the nonresonant background in this region.

Discussion

Vibrational enhancements occur when coupling between two resonances changes the intensities relative to the one-dimensional spectrum. DOVE-Raman enhancements occur for the CD_3CN 828 cm^{-1} and CH_3CN 917 cm^{-1} lines relative to the C_6D_6 line when they move through the region where $\omega_1 = \omega_{v''g}$ and $\omega_1 - \omega_2 = \omega_{vg}$. In this same region, there is another peak from a DOVE-IR double resonance that occurs when $\omega_1 = \omega_{v''g}$

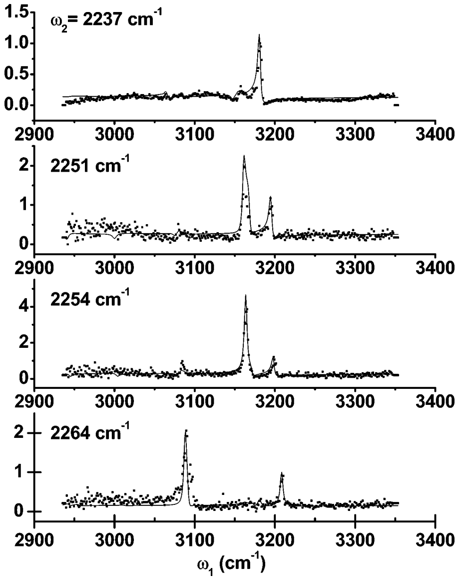

Figure 7. Nonlinear DOVE spectra where ω_1 was scanned for a series of ω_2 values over regions for the C−H stretch modes. The solid lines indicate simulated spectra from calculated values of $\chi^{(3)}$.

TABLE 3: Positions of the Doubly Vibrationally Enhanced Spectral Features in Acetonitrile and Deuteroacetonitrile

	DOVE-IR		DOVE-Raman		
	ω_1 (cm^{-1})	ω_2 (cm^{-1})	ω_1 (cm^{-1})	ω_2 (cm^{-1})	case
		CH_3CN			
$\nu_2 + \nu_4, \nu_2$	3164	2253	3164	2247	1
$\nu_3 + \nu_4, \nu_3 + 2\nu_4$	3201	2294	3201	2284	4
$\nu_2 + \nu_4, \nu_3 + \nu_4$	3164	2294			3
		CD_3CN			
$\nu_2 + \nu_4, \nu_2$	3089	2266	3089	2261	1

and $\omega_2 = \omega_{v'g}$. The DOVE-IR and DOVE-Raman peaks are offset by the anharmonicity: $\Delta\omega_2 = \omega_{v''g} - \omega_{v'g} - \omega_{vg}$.

The behavior of the different spectral features can be understood in terms of the DOVE processes. Table 3 summarizes the frequencies for the doubly resonant features for both DOVE-IR and DOVE-Raman processes in CH_3CN and CD_3CN with the frequencies for the simulations. The DOVE-Raman and DOVE-IR processes that occur at ($\omega_1 = 3164$, $\omega_2 = 2247$ cm^{-1}) and ($\omega_1 = 3164$, $\omega_2 = 2253$ cm^{-1}), respectively, for CH_3CN and ($\omega_1 = 3089$, $\omega_2 = 2261$ cm^{-1}) and ($\omega_1 = 3089$, $\omega_2 = 2266$ cm^{-1}), respectively, for CD_3CN are primarily responsible for the intensity and line shape changes seen in the spectra from $\omega_2 = 2238-2300$ cm^{-1}. The spectra are dominated by the strong DOVE-IR lines that appear at ($\omega_1 = 3164$, $\omega_2 = 2253$ cm^{-1}) and ($\omega_1 = 3089$, $\omega_2 = 2266$ cm^{-1}).

The sign of the interference between the nonlinear processes defines the line shapes. There are three behaviors in the data from Figure 5 that imply that the sign of $A_{\mathrm{DOVE-Raman}}$ in eq 8 must be opposite to that of A_{CARS}. The 828 and 917 cm^{-1} CARS lines are first suppressed by the DOVE-Raman process when $\omega_2 < (\omega_{v''g} - \omega_{vg})$ as seen in the disappearance of the 828 and 917 cm^{-1} lines when $\omega_2 = 2232$ cm^{-1}. The lines are then enhanced when $\omega_2 > (\omega_{v''g} - \omega_{vg})$, as seen in the 828 cm^{-1} line when $\omega_2 = 2269.9$ cm^{-1}. In addition, the CARS line shapes reverse their dispersion as seen in the 917 cm^{-1} line when $\omega_2 = 2239.1$ or 2244.2 cm^{-1} or less clearly in the 828 cm^{-1} line when $\omega_2 = 2251.5$ cm^{-1}. These changes agree with the behavior described in the theoretical section if $A_{\mathrm{DOVE-Raman}}/A_{\mathrm{CARS}} < 0$. This difference in sign also agrees with ab initio calculations of $\chi^{(3)}$.[15]

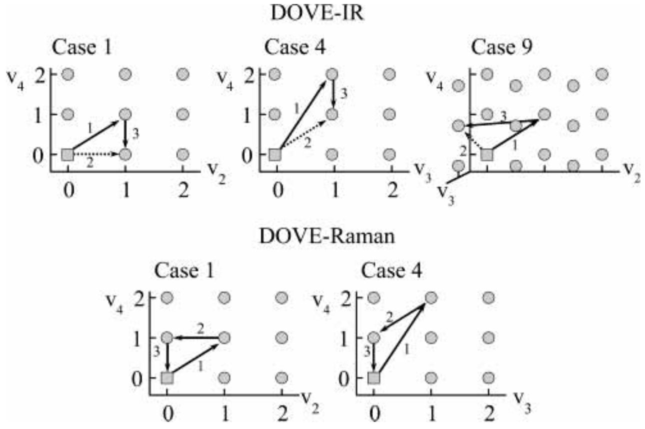

Figure 8. Example cases for the vibrational quantum number changes that occur in the two infrared and one Raman transition of a DOVE-IR or DOVE-Raman process.[28] Note that case 9 requires three axes so there are twice as many points as the other cases with only two axes.

Similar behaviors are seen for the 917 cm^{-1} line in spectra with $\omega_2 > 2260$ cm^{-1}. The spectra in this region are affected by an acetonitrile DOVE-Raman process that occurs when ($\omega_1 = 3201$, $\omega_2 = 2284$ cm^{-1}) and a DOVE-IR processes that occurs when ($\omega_1 = 3201$, $\omega_2 = 2294$ cm^{-1}). There is both a suppression of the 917 cm^{-1} line when $\omega_2 \approx 2258$ cm^{-1} because of the destructive interference between the CARS and DOVE-Raman process at ($\omega_1 = 3201$, $\omega_2 = 2284$ cm^{-1}) and an enhancement because of constructive interference with the DOVE-Raman process at ($\omega_1 = 3164$, $\omega_2 = 2247$ cm^{-1}). Then, an enhancement occurs at $\omega_2 \approx 2270$ cm^{-1} as the DOVE-Raman process at ($\omega_1 = 3201$, $\omega_2 = 2284$ cm^{-1}) begins to dominate. There is also a clear doubly resonant feature that develops when ($\omega_1 = 3163$, $\omega_2 = 2294$ cm^{-1}) from the DOVE-IR process involving ($\nu_2 + \nu_4$, $\nu_3 + \nu_4$) (see Table 3). This process requires coupling between the C−H bending motion and the C−N stretch. The presence of such coupling is confirmed by the presence of a combination band involving $\nu_2 + \nu_3$ in Table 2.

It is important to understand the changes in the vibrational quantum numbers that are required to observe DOVE processes. The changes for DOVE-IR and DOVE-Raman have been divided into eight cases that differ in the combination/overtone bands' involvement.[28] The features in Figure 4 and Table 3 contain examples of case 1, 3, and 4 processes. These cases are sketched in Figure 8. The three arrows connect the vibrational quantum numbers for the two coupled states (v_a and v_b) in the two infrared transitions and single Raman transition of a DOVE-IR or DOVE-Raman process. For example, the DOVE-IR feature at (ω_1, ω_2) = (3164, 2253 cm^{-1}) requires a pathway with the two infrared transitions where (v_2, v_4) = (0,0) → (1,1) and (0,0) → (0,1) and the Raman transition where (1,1) → (0,1). These transitions are represented by the arrows for case 1 in Figure 8. If one compares case 1 for DOVE-IR and DOVE-Raman, one sees both have $|\Delta v_2| = 1$ and $|\Delta v_4| = 1$, but there are two differences: $\Delta v_2 = +1$ and (v_2, v_4) = (1,1) → (1,0) for DOVE-IR, and $\Delta v_2 = -1$ and (v_2, v_4) = (0,1) → (0,0) for DOVE-Raman. In the absence of anharmonicity, the transition moments for DOVE-IR and DOVE-Raman should be identical for all three transitions. Case 4 in Figure 8 shows the quantum number changes of the DOVE processes associated with the $\nu_3 + \nu_4$ and $\nu_3 + 2\nu_4$ combination bands of modes ν_3 and ν_4 where similar arguments apply.

The third DOVE process ($\omega_1 = \nu_2 + \nu_4$, $\omega_2 = \nu_3 + \nu_4$) involves changes in modes ν_2, ν_3, and ν_4 and requires coupling between all three modes. The vibrational transitions are (ν_2, ν_3,

TABLE 4: Values Used for Simulations

states	$A_{\text{DOVE-IR}}(\Gamma_{v''\gamma} + \mathbf{\Gamma_{v'g}})/\mathbf{\Gamma_{v''v}\Gamma_{v''g}\Gamma_{v'g}}$	$A_{\text{DOVE-Raman}}/\Gamma_{v''g}\Gamma_{vg}$	$\lvert A_{\text{CARS}}/\Gamma_{vg}\rvert$	Γ_{cb} (cm^{-1})	$\lvert A_{NR}\rvert$	θ_{NR}
		CH_3CN				
$\nu_2 + \nu_4$, ν_2	−0.252	0.053		2.4		
$\nu_3 + \nu_4$, $\nu_3 + 2\nu_4$	−0.035	0.022		2.9		
$\nu_2 + \nu_4$, $\nu_3 + \nu_4$	−0.035			8.4		
ν_4			0.023			
		CD_3CN				
$\nu_2 + \nu_4$, ν_2	−0.163	0.059		2.7		
ν_4			0.023			
		C_6D_6				
ν_1			1.00			
		CH_3CN, CD_3CN, C_6D_6 Mixture				
					0.010	0.087π

ν_4) = (0,0,0) → (1,0,1), (0,0,0) → (0,1,1), and (1,0,1) → (0,1,1) for the two infrared combination band and a single Raman combination band transition, respectively. This case requires a three-dimensional diagram as shown in case 9 of Figure 8. It is similar to case 3 in Besemann et al.[28] in that the Raman transition is a combination band where the ν_4 mode remains in v = 1. This case contrasts with cases 1 and 4 because only the DOVE-IR process can occur. The analogous DOVE-Raman process requires an initial excited vibrational state population in the $\nu_2 + \nu_4$ state.[28]

These spectra can be modeled quantitatively by eq 8. The parameter values required for modeling the data are summarized in Tables 3 and 4. The line widths and dephasing parameters for all the coherences and the amplitudes for all the processes were determined by least-squares fitting of the experimental spectra. The amplitudes were normalized by the line widths of the single or double resonances so the peak intensity became independent of the line width. The amplitude values in Table 4 therefore are proportional to the peak intensity of any spectral feature relative to the C_6D_6 944 cm^{-1} line. For a single resonance, the tabulated values are A/Γ, while for DOVE-Raman and DOVE-IR, they are $A/\Gamma_{v''g}\Gamma_{vg}$ and $A(\Gamma_{v''g} + \Gamma_{v'g})/(\Gamma_{v''v'}\Gamma_{v''g}\Gamma_{v'g})$, respectively. Note that the inclusion of a SIVE resonance did not improve the simulations so the SIVE contributions were negligible. The predicted spectra are shown in Figure 5 as lines that are superimposed on the experimental data. The 2D simulation is also shown in Figure 6 for comparison with the experimental spectra. One can see excellent agreement across the entire range of frequencies.

The simulations were extended to the region of the C−H fundamental resonances and are shown as lines in Figure 7. The parameters for the C−H resonances were chosen from the calculated values of Kwak et al.[15] It can be seen that the calculated values produce lines that are too weak to be seen relative to the nonresonant background so these DOVE features could not be observed.

The modeling also allows one to visualize the interference that is responsible for the observed line shapes and relative intensities. Figure 9 shows the real and imaginary parts of the nonresonant, CARS, DOVE-Raman, and DOVE-IR $\chi^{(3)}$ values so one can see how they interfere to produce the signal's magnitude, $|\chi^{(3)}|$, in representative spectra. For example, one can see the real and imaginary parts of the CARS and DOVE-Raman features at $(\omega_1 - \omega_2) = 828$ and 917 cm^{-1} have opposite signs and will cancel when $\omega_2 = 2232$ cm^{-1}. They still cancel for the 828 cm^{-1} feature when $\omega_2 = 2244.2$ cm^{-1}, but the DOVE-Raman process has become enhanced enough to dominate the CARS process for the 917 cm^{-1} in this same spectrum. In addition, the imaginary part of the DOVE-Raman process has the opposite dispersion character from the real part of the CARS process so the observed line shape asymmetry reverses. The line shape change results in constructive interference between the 917 cm^{-1} DOVE-Raman and CARS features in the $\omega_2 = 2259.7$ cm^{-1} spectrum, but now there is also destructive interference with the DOVE-IR process that must be considered. The constructive interference is important in maintaining the intensity of both the 828 and 917 cm^{-1} features in the region between 2265 and 2300 cm^{-1}, but one must now consider the interference with the DOVE features from the resonances with the ($\omega_1 = \nu_3 + 2\nu_4$, $\omega_2 = \nu_3 + \nu_4$) and ($\omega_1 = \nu_2 + \nu_4$, $\omega_2 = \nu_3 + \nu_4$) states. These latter features are apparent in the $\omega_2 = 2292.4$ cm^{-1} spectra.

The modeling points out that a systematic error exists in the experimental spectral background because of a drift in the experimental parameters. The spectra were taken over a 2-week period and changes in the ratio of the background to the C_6D_6 944 cm^{-1} peak are evident. The changes are attributed to different relative contributions from the sample and the sample cell windows. The modeling required changes in the nonresonant background from a magnitude of 0.02 to 0.006 over the range from 2236 to 2303 cm^{-1}. Similar changes are evident from the periodic striping that appears in the 2D CMDVS spectra of Figure 2 in Murdoch et al.[16] The striping appears because several series of scans were made with interlacing ω_2 values so adjacent scans in the figure were taken on separate days but alternate scans were taken successively. The striping is not evident in the data for this paper because the data for successive ω_2 values were taken sequentially. Nevertheless, good agreement between simulations and experimental values could be achieved by adjusting the nonresonant background. The value in Table 4 is the average. This value is compatible with the estimates in previous publications.[9,11,15] If the previous estimates for the nonresonant backgrounds of CH_3CN and C_6D_6 are assumed and if the nonresonant background of CD_3CN is the same as that of CH_3CN, one predicts that the nonresonant background in Table 4 would be 0.014. The variations in the background may be responsible for hiding any SIVE contributions to the spectra.

There are a number of observations that should be made about the fitting values. The peak amplitudes of the main CH_3CN and CD_3CN DOVE-IR features are 28% and 22% of the C_6D_6 944 cm^{-1} Raman line. The difference in peak amplitudes is attributed to differences in the dephasing rates between CH_3CN and CD_3CN. In particular, the dephasing rate of the CD_3CN $v_2 + v_4$ combination band is appreciably larger than the same combination band in CH_3CN, and eq 8 shows that the larger rate causes a smaller peak amplitude.

Similarly, the DOVE-IR/DOVE-Raman amplitude ratios of the main features are −4.0 and −2.9 for CH_3CN and CD_3CN, respectively. Equation 12 predicts the DOVE-IR/DOVE-Raman ratio is −2 if the dephasing rates and transition moments are identical. For the dephasing rates in Table 4, the ratio would be −2.3 and −3.2. The CH_3CN ratio is appreciably different and may indicate the dephasing rates are inaccurate or the transition moments are not equal. The CD_3CN ratio is much closer.

The transition moments for DOVE-IR and DOVE-Raman could be different as can be seen from Figure 8. Although the transitions in DOVE-Raman and DOVE-IR involve the same changes in vibrational quantum numbers, the quantum numbers of the mode that is not changing in the transition differ, so anharmonicities can cause differences in the transition moments.

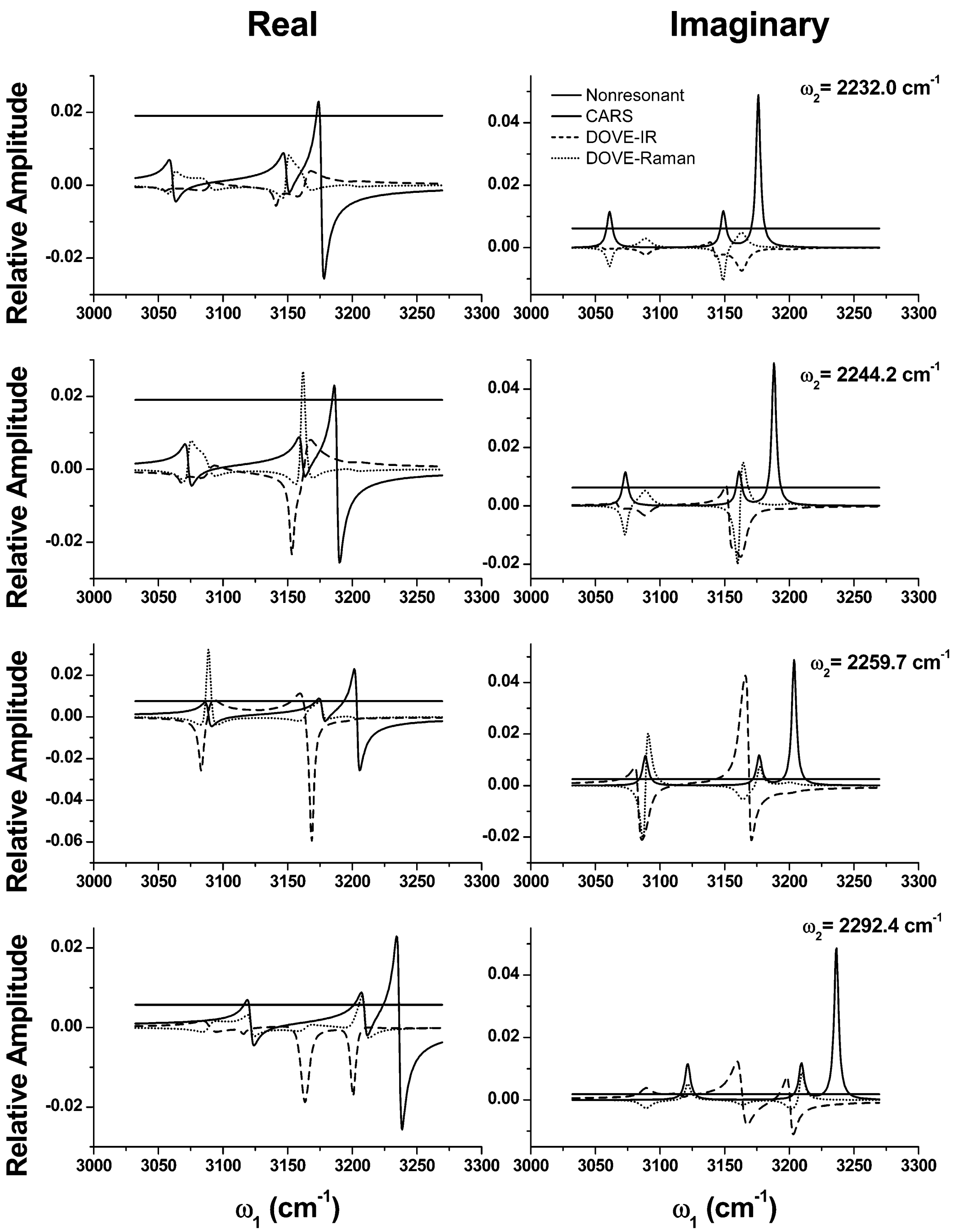

Figure 9. Real and imaginary values of $\chi^{(3)}$ are plotted in relative units for representative ω_2 values so one can see the relative importance of the nonresonant, CARS, DOVE-IR, and DOVE-Raman processes as well as visualize the interferences that are responsible for the observed intensities.

In particular, the transition moments for the (v_2, v_4) = (1,1) → (0,1) and (0,1) → (0,0) transitions of the main CH_3CN DOVE-Raman feature may be smaller than the (0,0) → (1,0) and (1,1) → (1,0) transitions of the main CH_3CN DOVE-IR feature. Justification for this difference, however, must await calculations.

It should also be noted that the CH_3CN DOVE-IR and DOVE-Raman features involving the $\nu_3 + 2\nu_4$ combination band have an amplitude ratio of −1.4. The ratio is presumably lower than the other DOVE features because $\Gamma_{vg}/\Gamma_{v''v'}$ is appreciably smaller than 1. Here, $\Gamma_{v''v'}$ may be increased by a larger population relaxation rate from the $\nu_3 + 2\nu_4$ combination band. The observed ratio agrees roughly with the −1.8 ratio expected from dephasing rates in Table 4, thus suggesting that the transition moments for the DOVE-IR and DOVE-Raman processes are similar for this case.

Equation 13 predicts that the DOVE-Raman and CARS processes destructively interfere and exchange dominance when $\Delta_{v''g} = -(A_{DOVE-Raman}/A_{CARS})$. The ν_4 mode's features become weak at this point and their line shape dispersive asymmetry changes. If the line widths are sufficiently narrow, this point occurs when ω_2 = 2228 and 2246 cm^{-1} for CH_3CN and CD_3CN, respectively. One can see that the changes in line shapes and intensities in Figures 5 and 6 are consistent with these positions.

Determination of $\chi^{(3)}$ Values

The values for the third-order susceptibility, $\chi^{(3)}$, are directly proportional to the *A* parameters in Table 4. Since the $\chi^{(3)}$ of the C_6H_6 ring-breathing Raman mode is known,[26,27] we can determine the $\chi^{(3)}$ for each process if we assume that C_6H_6 and C_6D_6 have the same $\chi^{(3)}$.[33] Some adjustments are necessary,

TABLE 5: $\chi^{(3)}$ Values[a]

	$\chi_{\mathrm{DOVE-IR}}$		$\chi_{\mathrm{DOVE-Raman}}$			
resonant states	measd	calcd	measd	calcd	χ_{CARS}	χ_{NR}
CH_3CN						
$\nu_2 + \nu_4, \nu_2$	-3.4×10^{-14}	-4.3×10^{-14}	7.1×10^{-15}	1.9×10^{-14}		
$\nu_3 + \nu_4, \nu_3 + 2\nu_4$	-4.6×10^{-15}	-8.5×10^{-15}	3.0×10^{-15}	4.7×10^{-15}		
$\nu_2 + \nu_4, \nu_3 + \nu_4$	-4.7×10^{-15}					
ν_4					3.1×10^{-15}	
CD_3CN						
$\nu_2 + \nu_4, \nu_2$	-2.2×10^{-14}	-3.9×10^{-14}	7.8×10^{-15}	1.2×10^{-14}		
ν_4					3.1×10^{-15}	
C_6D_6						
ν_1					1.3×10^{-13}	
Experimental Mixture						
						1.3×10^{-15}

[a] χ values are given in cubic centimeters per erg. Calculations assume N and F values of 6.73×10^{21} cm^{-3} and 4.04 for C_6D_6 and 1.97×10^{22} and 2.59 for CH_3CN, respectively.

however, because the C_6H_6 $\chi^{(3)}$ was measured by CARS with two visible laser frequencies that are significantly different from the three laser frequencies used in these experiments.[12–14] In addition, the value for the C_6H_6 $\chi^{(3)}$ will change in the sample mixture because the local field corrections and solvent density are different from the neat C_6H_6.

The $\chi^{(3)}$ dispersion is determined by the detuning of the laser frequencies from the electronic states that are associated with the C_6D_6. For singly resonant CARS, Bloembergen et al.[34] have shown the frequency dependence of the Raman $\chi^{(3)}$ is determined by 16 coherence pathways that can be combined to give

$$\chi_{\mathrm{R}}^{(3)} = \frac{NF}{6\hbar^3} \sum_{\mathrm{allstates}} \left[\frac{\mu_{\mathrm{ac}}^{(1)}\mu_{\mathrm{cb'}}^{(2)}}{\Delta_{\mathrm{ca}}^{(1)}\Delta_{\mathrm{b'a}}^{(1,-2)}} \left(\frac{\mu_{\mathrm{b'd}}^{(3)}\mu_{\mathrm{da}}^{(4)}}{\Delta_{\mathrm{da}}^{(4)}} - \frac{\mu_{\mathrm{ad}}^{(3)}\mu_{\mathrm{db'}}^{(4)}}{\Delta_{\mathrm{ad}}^{(3)}} \right) + \frac{\mu_{\mathrm{ac}}^{(3)}\mu_{\mathrm{cb'}}^{(2)}}{\Delta_{\mathrm{ca}}^{(3)}\Delta_{\mathrm{b'a}}^{(3,-2)}} \left(\frac{\mu_{\mathrm{b'd}}^{(1)}\mu_{\mathrm{da}}^{(4)}}{\Delta_{\mathrm{da}}^{(4)}} - \frac{\mu_{\mathrm{ad}}^{(3)}\mu_{\mathrm{db'}}^{(4)}}{\Delta_{\mathrm{ad}}^{(1)}} \right) + \frac{\mu_{\mathrm{ac}}^{(1)}\mu_{\mathrm{cb'}}^{(2)}}{\Delta_{\mathrm{ca}}^{(-2)}\Delta_{\mathrm{b'a}}^{(1,-2)}} \left(\frac{\mu_{\mathrm{b'd}}^{(3)}\mu_{\mathrm{da}}^{(4)}}{\Delta_{\mathrm{da}}^{(4)}} - \frac{\mu_{\mathrm{ad}}^{(3)}\mu_{\mathrm{db'}}^{(4)}}{\Delta_{\mathrm{ad}}^{(3)}} \right) + \frac{\mu_{\mathrm{ac}}^{(3)}\mu_{\mathrm{cb'}}^{(2)}}{\Delta_{\mathrm{ca}}^{(-2)}\Delta_{\mathrm{b'a}}^{(3,-2)}} \left(\frac{\mu_{\mathrm{b'd}}^{(1)}\mu_{\mathrm{da}}^{(4)}}{\Delta_{\mathrm{da}}^{(4)}} - \frac{\mu_{\mathrm{ad}}^{(1)}\mu_{\mathrm{db'}}^{(4)}}{\Delta_{\mathrm{ad}}^{(1)}} \right) \right] \quad (15)$$

where b′ is used to designate the Raman state and dephasing-induced processes are ignored. The superscripts indicate the laser fields associated with the transition moment and resonance detuning factor. The summation over all states can be avoided if we use the result of Asher and Johnson,[35] who found that the benzene Raman transition is dominated by the electronic transition at 52 500 cm^{-1}. If we use that state for the electronic resonances in eq 15 and the known parameters for the C_6D_6 Raman transition, we calculate that $\chi_{\mathrm{R}}^{(3)}$ for the ω_i values of our experiment is 2.22× smaller than the $\chi_{\mathrm{R}}^{(3)}$ in the Levenson and Bloembergen experiments.[26,27] The largest correction is the factor of 2 in the formal definition of $\chi^{(3)}$ between three laser experiments and two laser experiments where $\omega_1 = \omega_3$.[36] There is an additional 11% correction because of the differences in the detuning of the ω_1 and ω_2 pair of excitations in our experiment and the ω_3 and ω_4 pair. The amplitude contributed by the most resonant pathways decreases because the ω_1 and ω_2 pair is farther from resonance with the excited electronic state. The amplitude contributed by the antiresonant pathways can increase because the ω_1 and ω_2 pair does not move as far from resonance. The net effect is an 11% decrease in the $\chi_{\mathrm{R}}^{(3)}$.

The C_6D_6 $\chi^{(3)}$ values depend on the local field and concentration, F and N, for neat C_6D_6, but these values will change when C_6D_6 is used as an internal standard in the acetonitrile/deuterioacetonitrile mixture. Since the hyperpolarizability is independent of the local field and concentration, the values of A in Table 4 will represent the ratio of the nonlinear hyperpolarizabilities to the C_6D_6 hyperpolarizability. Thus, the first step in determining the DOVE $\chi^{(3)}$ values is use of the A ratios in Table 4 along with the C_6D_6 hyperpolarizability to obtain the DOVE hyperpolarizabilities. One can then convert the hyperpolarizabilities to $\chi^{(3)}$ values from the F and N_i in the mixture.

From eq 8, the peak $\chi^{(3)}$ of each contribution depends on N, F, A, and Γ for each component and nonlinear process. The C_6D_6 values for N_i and F of the sample and the neat solution are tabulated in Table 5 along with the CH_3CN and CD_3CN values for the sample. Together with the A and Γ values in Tables 3 and 4, the peak $\chi^{(3)}$ values of the C_6D_6 internal standard can be related to the peak $\chi^{(3)}$ values of each process of each component. Table 5 summarizes these values. The CH_3CN values in Table 5 that result from fitting the frequency domain spectra agree with the values determined earlier from the concentration dependence of the acetonitrile/deuteriobenzene samples.[9]

The peak DOVE $\chi^{(3)}$ values can be estimated from the molar absorptivities of the two single-photon infrared absorption transitions and the peak Raman cross-section for the two photon Raman process. These transitions provide the transition moments required for determining the $\chi^{(3)}$ values.[9] For example, the peak infrared absorption coefficient and peak Raman $\chi^{(3)}$ are

$$\alpha_{\mathrm{v'g}} = \frac{4\pi\omega_{\mathrm{v'g}} N F_{\mathrm{v'g}} \mu_{\mathrm{v'g}}^2 \rho_{\mathrm{gg}}}{\hbar c \Gamma_{\mathrm{v'g}}} \quad (16)$$

$$\chi_{\mathrm{vgRaman}}^{(3)} = \frac{-iNF_{\mathrm{eg}}^2 F_{\mathrm{ev}} \mu_{\mathrm{eg}}^2 \mu_{\mathrm{ev}}^2 \rho_{\mathrm{gg}}}{4D_{\mathrm{Raman}} \hbar^3 |\Delta_{\mathrm{eg}}|^2 \Gamma_{\mathrm{vg}}} \quad (17)$$

where $\Delta_{\mathrm{eg}} \equiv \omega_{\mathrm{eg}} - \omega_1 - i\Gamma_{\mathrm{eg}}$ and $\omega_1 = \omega_3$. D_{Raman} is 3 for a two-laser experiment and 6 for a three-laser experiment. Solving for the transition moments and substituting into the peak DOVE-IR $\chi^{(3)}$

$$\chi_{\mathrm{DOVE-IR}}^{(3)} = \frac{NF_{\mathrm{v'g}} F_{\mathrm{v''g}} F_{\mathrm{ev''}} \mu_{\mathrm{v''g}} \mu_{\mathrm{v'g}} \mu_{\mathrm{v''e}} \mu_{\mathrm{ev'}} \rho_{\mathrm{gg}}}{4D_{\mathrm{DOVE}} \hbar^3 \Gamma_{\mathrm{v'g}} \Gamma_{\mathrm{v''g}} \Delta_{\mathrm{ev'}}} \left(1 - \frac{\Gamma_{\mathrm{v''v'}}^{\mathrm{g}}}{\Gamma_{\mathrm{v''v'}}}\right) \quad (18)$$

one finds

$$\chi^{(3)}_{\mathrm{DOVE-IR}} = \frac{c\left(1 - \frac{\Gamma_{\mathrm{v''v'}}{}^{\mathrm{g}}}{\Gamma_{\mathrm{v''v'}}}\right)\Delta_{\mathrm{eg}}}{8\pi D_{\mathrm{DOVE}}\Delta_{\mathrm{ev'}}}\sqrt{\frac{i\hbar F_{\mathrm{v'g}}F_{\mathrm{v''g}}F_{\mathrm{ev''}}{}^{2}D_{\mathrm{Raman}}\alpha_{\mathrm{v'g}}\alpha_{\mathrm{v''g}}\chi^{(3)}_{\mathrm{Raman}}\Gamma_{\mathrm{vg}}}{F_{\mathrm{ev'}}F^{2}_{\mathrm{eg}}\omega_{\mathrm{v'g}}\omega_{\mathrm{v''g}}\Gamma_{\mathrm{v'g}}\Gamma_{\mathrm{v''g}}N\rho_{\mathrm{gg}}}} \tag{19}$$

where $\Gamma^{\mathrm{g}}_{\mathrm{v''v'}} = \Gamma_{\mathrm{v''v'}} - \Gamma_{\mathrm{v'g}} - \Gamma_{\mathrm{v''g}}$, c is the speed of light, F is the local field factor, N is the number density, and D is a degeneracy factor. The sign of $\chi^{(3)}$ is not defined in these relations because the α and $\chi_{\mathrm{Raman}}{}^{(3)}$ are insensitive to the sign of the transition moments. The absorption coefficients are easily measured and tabulated in Table 5. We also assume that $\chi_{\mathrm{Raman}}{}^{(3)}$ is the same as the 3 laser $\chi_{\mathrm{CARS}}{}^{(3)}$ since the dispersion of $\chi^{(3)}$ should be smaller than that of C_6D_6. Substituting the known values of the experimental parameters into eq 19 predicts the DOVE-IR values shown in Table 5. These values are in reasonable agreement with the experimentally measured values. The agreement gives confidence that one can estimate the multiply vibrationally resonant $\chi^{(3)}$ values from conventional spectra.

Conclusions

The line shapes of CMDVS spectra reflect the underlying quantum interferences between the different nonlinear processes. The dephasing-induced resonances play a dominant role in defining line shapes. In particular, the interferences between nonlinearities make the DOVE resonances sharper and narrower than the star-shaped Lorentzian lines expected from a single coherence pathway. Since the relative contributions from the different pathways depend on the differences in the dephasing rates and the transition moments, the line shapes provide information about the dephasing of both single and double quantum coherences that are involved in each pathway. In addition, each process has a characteristic spectral signature that allows identification and measurement of its contribution. A detailed modeling of the experimental data provides quantitative values for the molecular parameters defining this model system. Furthermore, the third-order susceptibilities of each nonlinear process can also be obtained by comparison with a deuteriobenzene internal standard. The measured values agree with estimates obtained from the relating the third-order susceptibilities to the molar absorptivities and Raman cross-sections of the transitions involved in the nonlinearity.

Acknowledgment. This work was supported by the National Science Foundation under grant CHE-0130947. Acknowledgment is also made to the donors of the Petroleum Research Fund of the American Chemical Society for their support of this research.

References and Notes

(1) Mukamel, S. *Annu. Rev. Phys. Chem.* **2000**, *51*, 691.
(2) Wright, J. C. *Int. Rev. Phys. Chem.* **2002**, *21*, 185.
(3) Scheurer, C.; Mukamel, S. *Bull. Chem. Soc. Jpn.* **2002**, *75*, 989.
(4) Scheurer, C.; Mukamel, S. *J. Chem. Phys.* **2002**, *116*, 6803.
(5) Asplund, M. C.; Zanni, M. T.; Hochstrasser, R. M. *Proc. Natl. Acad. Sci. U.S.A.* **2000**, *97*, 8219.
(6) Zanni, M. T.; Cnanakaran, S.; Stenger, J.; Hochstrasser, R. M. *J. Phys. Chem. B* **2001**, *105*, 6520.
(7) Bonn, M.; Hess, C.; Miners, J. H.; Heinz, T. F.; Bakker, H. J.; Cho, M. *Phys. Rev. Lett.* **2001**, *86*, 1566.
(8) Cho, M. *J. Chem. Phys.* **2000**, *112*, 9002.
(9) Zhao, W.; Wright, J. C. *Phys. Rev. Lett.* **1999**, *83*, 1950.
(10) Zhao, W.; Wright, J. C. *J. Am. Chem. Soc.* **1999**, *121*, 10994.
(11) Zhao, W.; Wright, J. C. *Phys. Rev. Lett.* **2000**, *84*, 1411.
(12) Labuda, M. J.; Wright, J. C. *Phys. Rev. Lett.* **1997**, *79*, 2446.
(13) LaBuda, M. J.; Wright, J. C. *Chem. Phys. Lett.* **1998**, *290*, 29.
(14) LaBuda, M. J.; Wright, J. C. *J. Chem. Phys.* **1998**, *108*, 4112.
(15) Kwak, K.; Cha, S.; Cho, M.; Wright, J. C. *J. Chem. Phys.* **2002**, *117*, 5675.
(16) Murdoch, K. M.; Condon, N. J.; Zhao, W.; Besemann, D. M.; Meyer, K. A.; Wright, J. C. *Chem. Phys. Lett.* **2001**, *335*, 349.
(17) Prior, Y.; Bogdan, A. R.; Dagenais, M.; Bloembergen, N. *Phys. Rev. Lett.* **1981**, *46*, 111.
(18) Andrews, J. R.; Hochstrasser, R. M. *Chem. Phys. Lett.* **1981**, *83*, 427.
(19) Wright, J. C.; Carlson, R. J.; Hurst, G. B.; Steehler, J. K.; Riebe, M. T.; Price, B. B.; Nguyen, D. C.; Lee, S. H. *Int. Rev. Phys. Chem.* **1991**, *10*, 349.
(20) Mukamel, S. *Principles of Nonlinear Optical Spectroscopy*, 1st ed.; Oxford University Press: New York, 1995.
(21) Wright, J. C.; Carlson, R. J.; Riebe, M. T.; Steehler, J. K.; Nguyen, D. C.; Lee, S. H.; Price, B. B.; Hurst, G. B. Fully Resonant Nondegenerate Nonlinear Mixing Spectroscopy. In *Vibrational Spectroscopy and Structure*, 1st ed.; Bist, H. D., Durig, J. R., Sullivan, J. F., Eds.; Elsevier Science Publishers: Amsterdam, 1989; Vol. 17B; p 123.
(22) Mukamel, S. *J. Chem. Phys.* **1985**, *82*, 5398.
(23) Lee, D.; Albrecht, A. C. *Advances in Infrared and Raman Spectroscopy*, 1st ed.; Wiley-Heyden: Chichester, U.K., 1985; Vol. 12.
(24) Wright, J. C.; Chen, P. C.; Hamilton, J. P.; Zilian, A.; LaBuda, M. J. *Appl. Spectrosc.* **1997**, *51*, 949.
(25) Chen, P. C.; Hamilton, J. P.; Zilian, A.; LaBuda, M. J.; Wright, J. C. *Appl. Spectrosc.* **1998**, *52*, 380.
(26) Levenson, M. D.; Bloembergen, N. *J. Chem. Phys.* **1974**, *60*, 1323.
(27) Levenson, M. D.; Bloembergen, N. *Phys. Rev. B* **1974**, *10*, 4447.
(28) Besemann, D. M.; Condon, N. J.; Murdoch, K. M.; Meyer, K. A.; Zhao, W.; Wright, J. C. *Chem. Phys.* **2001**, *266*, 177.
(29) Tolles, W. M.; Nibler, J. W.; McDonald, J. R.; Harvey, A. B. *Appl. Spectrosc.* **1977**, *31*, 253.
(30) Zhao, W.; Murdoch, K. M.; Besemann, D. M.; Condon, N. J.; Meyer, K. A.; Wright, J. C. *Appl. Spectrosc.* **2000**, *54*, 1000.
(31) Wright, J. C.; Zhao, W.; Murdoch, K. M.; Besemann, D. M.; Condon, N. J.; Meyer, K. A. Nonlinear 2D Vibrational Spectroscopy. In *Handbook of Vibrational Spectroscopy*; Chambers, J. M., Griffiths, P. R., Eds.; John Wiley and Sons: New York, 2001.
(32) Venkateswarlu, P. *J. Chem. Phys.* **1951**, *19*, 293.
(33) Fernandez-Sanchez, J. M.; Montero, S. *J. Chem. Phys.* **1989**, *90*, 2909.
(34) Bloembergen, N.; Lotem, H.; Lynch, R. T. *Indian J. Pure Appl. Phys.* **1978**, *70*, 151.
(35) Asher, S. A.; Johnson, C. R. *J. Phys. Chem.* **1985**, *89*, 1375.
(36) Orr, B. J.; Ward, J. F. *Mol. Phys.* **1971**, *20*, 513.
(37) Bertie, J. E.; Lan, Z. *J. Phys. Chem. B* **1997**, *101*, 4111.